Materials and Design 160 (2018) 1281–1294

Contents lists available at ScienceDirect

Materials and Design

journal homepage: www.elsevier.com/locate/matdes

Compressive performance of an arbitrary stiffness matched anatomical Ti64 implant manufactured using Direct Metal Laser Sintering

Aaron Vance *, Klaudio Bari, Arun Arjunan

School of Engineering, Faculty of Science and Engineering, University of Wolverhampton, Telford Campus, Telford TF2 9NT, United Kingdom

HIGHLIGHTS

- A Ti6Al4V tibial implant that mimics the segmented bone anatomy is presented.
- The compressive properties of Ti6Al4V cellular anatomical structure was investigated.
- Finite Element Analysis was carried out for unit cell selection and performance prediction.
- An additively manufactured segmental bone repair implant with Young's modulus slightly lower than bone.

GRAPHICAL ABSTRACT

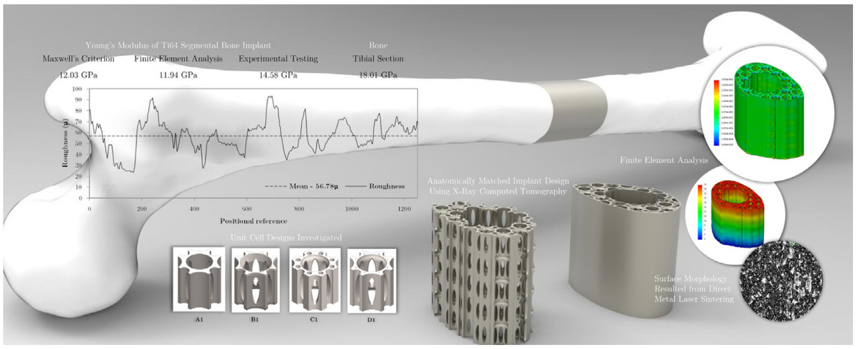

ARTICLE INFO

Article history:
Received 14 July 2018
Received in revised form 24 September 2018
Accepted 2 November 2018
Available online 8 November 2018

Keywords:
Segmental Bone Defect (SBD)
Stiffness matching
Direct Metal Laser Sintering
Finite Element Analysis
Sheathed cellular structure
3D printing
Compression testing

ABSTRACT

The reduction of stress shielding following Segmental Bone Defect (SBD) repair requires stiffness matching strategies. Accordingly, this work introduces a Ti6Al4V (Ti64) SBD tibial implant that mimics the segmented bone anatomy using a digital bio-model derived from X-Ray μCT Scan data. The implant features a sheathed periodic unit cell design that can perform slightly lower than the segmented bone being replaced for potential stiffness matching. Finite Element Analysis (FEA) was carried out for the selection of unit cell and to predict the implant performance. The results were then compared to compression test data from a Ti64 Grade 23 implant manufactured using Direct Metal Laser Sintering (DMLS) to assess predictability. The outcome of this research shows an anatomical stiffness matched design that maybe suitable for SBD repair of a tibial segment that can be manufactured using DMLS. The developed implant exhibits Young's Modulus (E) of 12.03, 11.94 and 14.58 GPa using Maxwell's criterion, FEA and experimental (highest) methodologies respectively. This is slightly lower than the segmented bone that exhibited 18.01 GPa (E_{Tibia}) to allow for stiffness matching following a period of osseointegration depending on 'critical size'. Furthermore, the surface roughness of the implant was found to be favourable for osteoblasts attachment.

1. Introduction

Segmental Bone Defect (SBD) repair of defective bone remains a challenge due to complications that arises from anatomical mismatch and bone reintegration due to stress shielding [1]. Additive Manufacturing (AM) enables tailored porous material to be designed with desirable mechanical properties [2]. This is primarily due to the effectiveness of

---

* Corresponding author at: School of Engineering, Faculty of Science and Engineering, University of Wolverhampton, Telford Campus, Shifnal Road, Priorslee, Telford TF2 9NT, United Kingdom.
E-mail address: a.vance@wlv.ac.uk (A. Vance).

https://doi.org/10.1016/j.matdes.2018.11.005

the process to deliver open or closes cellular architecture with dimensional accuracy [3]. Historically orthopaedic implants have been manufactured using cast or forged solid pieces of metal, that are 4–8 times stiffer than natural bone. These traditional manufacturing processes were a barrier to generating complex geometrical cellular features that can vary the strength of Ti64 implants to make the implant perform like bone [4].

Previous studies have shown that cellular structure architecture can affect both mechanical and bio-compatibility properties [5]. The biocompatibility of commercially used Ti64 titanium alloy (Ti6Al4V) is well founded in medical environments [6,7]. However, the use of traditional Ti64 implants in-vivo presents mechanical property mismatch due to the phenomenon of stress shielding [8–12]. This is primarily due to the significant difference between the Young's Modulus, of Ti64 (≈115 GPa) and the corresponding value of the bone to be replaced, which is generally in the range of 18.6 to 20.7 GPa for cortical bone [13].

This stiffness mismatch between Ti64 and segmented bone is detrimental to bone–implant assembly and often leads to bone resorption, osteopenia, loosening of the implant, premature bone fracture and the reduction of bone density [14,15]. The solution to this is to avoid stress shielding by developing implants that can match the stiffness of the bone [16] after a period of bone regrowth by promoting osseointegration [17,18]. For titanium-based alloys, numerous research efforts are evident in published tissue engineering literature [19–21]. However, attempts on implant-based SBD repairs in long bone close to 2 cm [22] shows that large amounts of bone will not grow into such an implant above ‘critical size’ [23,24] despite effective porosity. Consequently, the standard of care for segmental, critical size, bone defects is autologous bone graft [25]. Furthermore, achievements have also been made in design of scaffolds that mimic the mechanical behaviour of natural bone. However, these methodologies do not consider the global anatomical geometry of the segmented bone coupled with potential stiffness matching strategies.

A further criterion that is often omitted when considering implant performance is maladapted stress concentration. Tibial bone cross-section is a dynamic structure that has the capacity to respond to physical stimuli as mentioned by Eckstein et al. [26]. Due to this, tibial bone area is prone to cartilage defects and cartilage volume loss in certain cases [27], whereby the bone area appears maladaptive due to stress concentration from disproportionate load transmission [28]. However, during adolescence and childhood stimulus due to exercise or physical activity leads to increased cortical bone size, leading to increased bone mass [29]; therefore, increased bone area during growth may reflect adaptive change. Accordingly, to reduce maladapted stress concentration, it is fundamental that the implant introduced into the host bone do not contribute to disproportionate load transmission. While this required the implant performance to be studied in conjunction with the host-bone as single continuum bodies with contact areas carefully modelled, this study only considers implant stiffness in isolation which is a key limitation that warrant mentioning.

Developments of AM techniques have enabled the successful production of metallic scaffolds and other complex geometries in titanium-based alloys [30]. Particularly, the Direct Metal Laser Sintering (DMLS) have solved key manufacturing challenges such as micro-scale cellular geometry, and functional grading [31,32]. The structure of bone tissues is naturally heterogeneous and complex. Consequently, efforts have been placed to develop implants focusing on the creation of simplified models which are functionally similar to the host bones [33].

X-Ray Computed Tomography (CT) can improve implant design by providing key insight into anatomical architecture. CT technologies are well founded within medical and engineering sectors [34], enabling the generation of three-dimensional (3D) bio-models [17,18,35]. Coupling this with AM can enable the production of anatomical products derived from bespoke bio-models. Furthermore, additively manufactured meta-biomaterials have shown to improve bone regeneration and osseointegration [5].

Practical SBD repair implant designs include regular structures with controllable geometries and irregular anatomic architecture. However, the anatomic architecture derived from CT or MRI images feature random porosity and microstructural features that are challenging to manufacture [36]. Consequently, the alternative approach is to model regular cellular structures using Computer Aided Design (CAD) tools [37,38].

These CAD generated cellular models for bone implants often feature a base unit cell, that is then multiplied to obtain the desired global geometry. Regular cubic, honeycomb matrix, octahedral unit and Kelvin cells has been widely used in the designs of various implants [16,39]. However, most of these implants feature open cellular non-anatomic design that are safety critical due to geometrical animalities such as tapered ends.

The mechanical properties of cellular structures at micron (μm) levels are highly correlated with the unit cell and the manufacturing process. Consequently, it is important to have a design with predictable behaviour to optimise manufacturing parameters and to ensure repeatability. Numerical simulations based on the Finite Element Method (FEM) are often employed to predict the behaviour of cellular structures considering the geometrical complexity. In most cases Finite Element Analysis (FEA) was used to predict the effective Modulus and associated mechanical behaviour. These properties were then validated using mechanical tests to estimate percentage error for further extrapolation [40,41]. The validated FEA data can be further compared to investigate the effects of manufacturing techniques on implant performance.

For honeycomb inspired cellular structures, works of Chen et al. [42,43] has enabled the understanding of both the thermal and compressive behaviour. The studies showed that bio-inspired ‘Kagome’ [44] and Triangular hierarchical honeycombs exhibit improved specific stiffness in comparison to regular honeycomb cellular structures. While the outcomes cannot be directly linked to the application of bone implants; the associated design parameters are transferable for potential stiffness matching strategies and is worth exploring.

At a material level commercially, pure titanium (Ti) is also receiving attention in medical applications. The key limiting factor in this regard was the requirement for improved mechanical properties biomechanical compatibility. However, pioneering works by Attar et al. [45] has manipulated AM parameters with Ti grain size range up to 100 μm to produce fully dense parts that do not require post-treatments resulting in improved compressive strength (1136 MPa). This shows the potential of AM parameters in optimising the structural performance of Ti based alloys. Strength characteristics of open square cellular structures manufactured using AM were investigated under uniaxial compression by Parthasarathy et al. [46]. Here the strength was dependent on the strut size and no weakness of connecting layers was observed.

While unsheathed cellular designs offer high level of customisation for Ti64 to match the Young's Modulus of the host bone, this is not without potential safety risks. Metal debris can be released from the tapered junction in open cellular designs that can cause adverse soft tissue reactions once implanted [47]. To this aspect, there is significant gap in the literature relating to the mechanical performance of both sheathed and anatomical implants which this study attempts to contribute. While, mimicking the host bone geometry in a SBD repair is not a requirement doing so may be advantageous. The usual approach is to develop implant design that match the stiffness while un-interrupting the normal loading pattern of a healthy bone in a biocompatible material that does not lead to infection. However, this research was exploratory in the sense that, it aided the understanding of the compressive behaviour of an arbitrary anatomical implant design that feature stiffness matching strategy.

It was interesting to explore the aspect of anatomically matched geometry as it was thought to support the natural load transfer with the host bone. Furthermore, where the dimensions of the segmental defect considered are arbitrary, the bone to implant contact area may be enhanced due to the anatomical match of the contact surfaces. Lastly the aspect of coupling anatomical geometry with cellular structure stiffness-matching provided non-uniform radial grading due to the difference in cell-size imposed by the anatomy. In any case, the compressive behaviour of an implant that combine anatomical and stiffness matching strategy was unavailable in literature leaving a knowledge gap. Accordingly, for the first time, this paper presents the mechanical performance of a sheathed but cellular anatomical Ti64 implant featuring an arbitrary length but avoids topological taper at the same suitable for stiffness matching. Furthermore, the strategy to mimic the anatomical shape of the segmented bone utilising both X-Ray CT and DMLS [48] technologies is also demonstrated. This is done through the generation of a bespoke bio-model of the tibial segment and placing linearly multiplied unit cells to match the anatomical profile. FEA was then performed to predict the performance of the implant under compression and to quantify the effect of the DMLS manufacturing process. Under identical boundary conditions, mechanical tests were performed to validate the numerical results. The implant prototype was further characterised using Confocal Laser Scanning Microscopy (CLSM) to investigate the surface roughness and microstructure respectively. It is hypothesised that the design and manufacturing methodology will provide Ti64 anatomical sheathed SBD repair implants with Modulus slightly lower than the segmented tibia. It is proposed that the implant manufactured using DMLS could have the potential to improve the load transfer to the host bone and improve the longevity of Ti64 SBD repair implant.

2. Materials and methods

2.1. Generation of anatomical profile

From the tibia bone shown in Fig. 1a, an arbitrary section was cut using a rotary saw blade. The selection of the arbitrary length was inspired from the works of Reichert et al. [22] where a Tibial Segmental Bone Defect of 2 cm was replaced entirely with a composite scaffold. Nevertheless, it must be noted that that large amounts of bone cannot grow along a length of 21.2 mm length as it is over the "critical size" at which the body cannot heal unaided as established by Schmitz and Hollinger [23]. Accordingly, the selection of the 'segmental length' was purely arbitrary and is not representative of an actual defect that the implant tries to intervene in practice. Instead, the research is exploratory to understand the compressive performance while combining the anatomical profile with cellular stiffness matching strategy. Nevertheless, it is anticipated that the results can have impact on anatomical tissue engineering scaffolds and related research in the wider context.

The resulting segmented bone section (Fig. 1b) was scanned using the Bruker Skyscan2211 X-Ray CT scanner to generate the segmented bone topography. Even though the process created a fine resolution 3D model, for computational efficiency only the surface topography was extracted in the form of Standard Tessellation Language (STL). The STL file was imported to SolidWorks 2018 and replicated into a fully dense solid bio-model as shown in Fig. 1c using Bézier splines. This model was used to generate volumetric data that later informed the unit cell design calculations.

2.2. Unit cell and global implant design

A bottom up modelling approach using SolidWorks 2018 was employed to generate a singular unit cell. Four variants of the unit cell designs were considered for initial analysis as shown in Fig. 2. The design of the unit cell started with the cross-sectional area of 100 mm^2 and a height of 10 mm resulting in a bulk volume of 1000 mm^3.

Fixing the numbers of beams and joints as constant and using the bulk material density of Ti64 (0.0044 g/mm^3), each unit cell exhibited a mass (m_{uc}) of 1.27, 1.03, 1.12 and 1.09 g for A1, B1, C1 and D1 respectively. The resultant unit cell densities were (ρ_{uc}) 0.0013 (A1), 0.0010 (B1), 0.0011 (C1), 0.0011 (D1) g/mm^3. The unit cell designs were analysed and compared in terms of both relative densities (0.2868 (A1), 0.2326 (B1), 0.2529 (C1), 0.2461 (D1)) and stress profile. Based on the results the best performing unit cell was selected to design the anatomical SBD implant shown in Fig. 3. The implant geometry shown in Fig. 3a was generated by triaxial linear patterning of the best performing unit cell. Using the 'Boolean Combine' and 'difference' functions the unit cell geometries were combined to form a single part.

Investigating the unsheathed design (Fig. 3a), it became apparent that the open cell design was non-practical due to tapered section and sharp corners; both of which are considered safety critical [47]. Furthermore, the unsheathed design exhibited anatomical mismatch along the circumferential topology which was outside the scope of this study. Consequently, only the sheathed design shown in Fig. 3b was considered for further analysis. However, it must be noted that the sheathed design combines a non-uniform cell geometry due to the anatomical topology.

2.3. Finite Element Analysis

Three-dimensional (3D) FEA were carried out using the SolidWorks 2018 simulation suite on all unit cell designs (Fig. 2) as well as the sheathed implant design (Fig. 3b). While the FEA on unit cells advised on the best performing cellular geometry for the SBD implant, the simulation data from the sheathed model assisted in quantifying the effect of the manufacturing process on the compressive performance.

Even though a mixed elemental matrix was used, the mesh primarily featured a three-node Triangular shell element. Using a mesh sensitivity

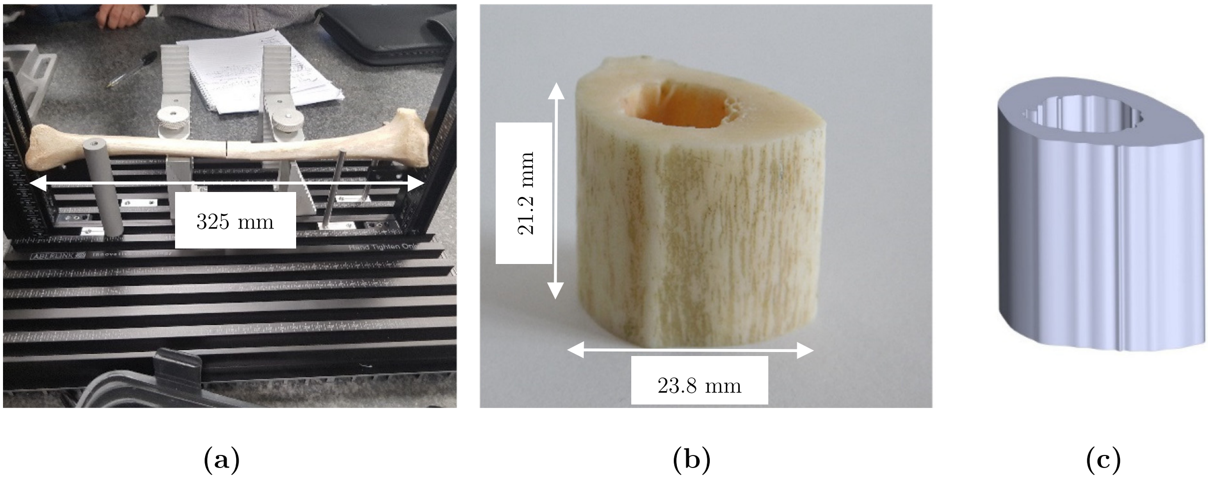

Fig. 1. Anatomical profile generation showing (a) tibial bone considered, (b) segmented section and (c) fully dense CAD bio-model based on X-Ray CT Scan data of the segmented bone.

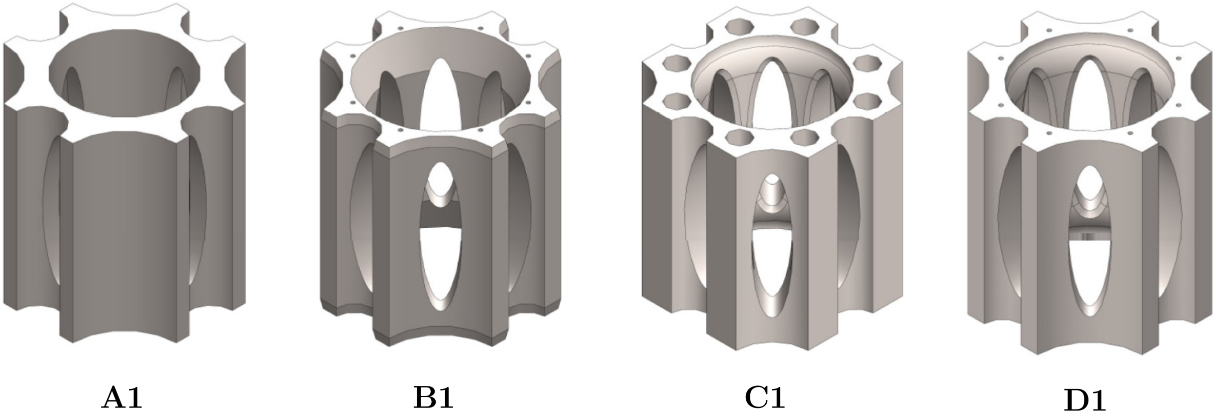

Fig. 2. Unit cell variants considered for initial analysis.

analysis, further mesh refinements were carried out until the von Mises criteria converged within 5% error. The resulted elemental and nodal distribution for the converged finite element model along with associated solution time is listed in Table 1. The elemental matrix was solved using an Intel Core i7-6700 CPU at 3.40 GHz with a maximum RAM allocation of 32 GB.

The boundary conditions were applied to replicate the physical test conditions as shown in Fig. 4. The bottom surface of the implant was fully constrained in Uy (displacement normal to load) and a perfectly axial load was applied at the top face. To simulate the unit cell the load (F_{UA}) applied was the product of the ratio of the area of unit cell (A_{UA}) to the area of bone (A_{Bone}) and a 1 kN axial force. For the implant, the force ($F_{Implant}$) applied was the product of the ratio of the area of the implant ($A_{Implant}$) to the area of bone (A_{Bone}) and a 1 kN axial force. The resultant force was 555.49 N and 1 kN to simulation the unit cells and implant respectively.

The cellular structures were modelled as single continuum bodies, which were assigned Ti64 Bulk material properties. The non-linear material behaviour was modelled using the bilinear isotropic hardening stress–strain (BISO) relationship based on bulk material data obtained from data sheet [49]. The BISO material model was selected due to its capacity to efficiently capture the elastic-plastic behaviour of additively manufactured cellular structures under minimal solution time [50]. The material model featured a Young's Modulus (E_B) of 104.8 GPa, Yield strength of 1.14 GPa, Ultimate strength of 1.43 GPa, density of 4428.78 kg/m^3 and Poisson's ratio of 0.342. From the FEA results, Eq. (1) was used to predict the effective Modulus (E_{FEA}) of the sheathed implant. Where, E_{UC} is the relative Modulus of the unit cell used for the implant design, σ_{FEA} is the maximum stress and ε_{FEA} is the maximum strain, which is the ratio of the maximum deflection from FEA (mm) to original length (21.2 mm).

$$E_{FEA} = \frac{E_{UC}}{E_B} \times \frac{\sigma_{FEA}}{\varepsilon_{FEA}} \tag{1}$$

2.4. Implant manufacture

The implant design was exported into STL file format and subsequently into Materialise Magics. Supporting structures were generated by the software where overhangs were >45° angle. The parts were printed using EOS M290, DMLS 3D Printer. Build plate additional support was generated at 1 mm and removed using submerged wire Electro-Discharge Machining (EDM). Laser sintering was performed using Ytterbium fibre laser system that uses Ti64 particles 25–40 μm in diameter. The laser scanning speed was 7 m/s at a wavelength of 1054 nm and laser spot size of 40 μm was used. The implant design was based on D1 and was heat-treated at 650 °C for 3 h under a controlled Argon environment after the sintering process.

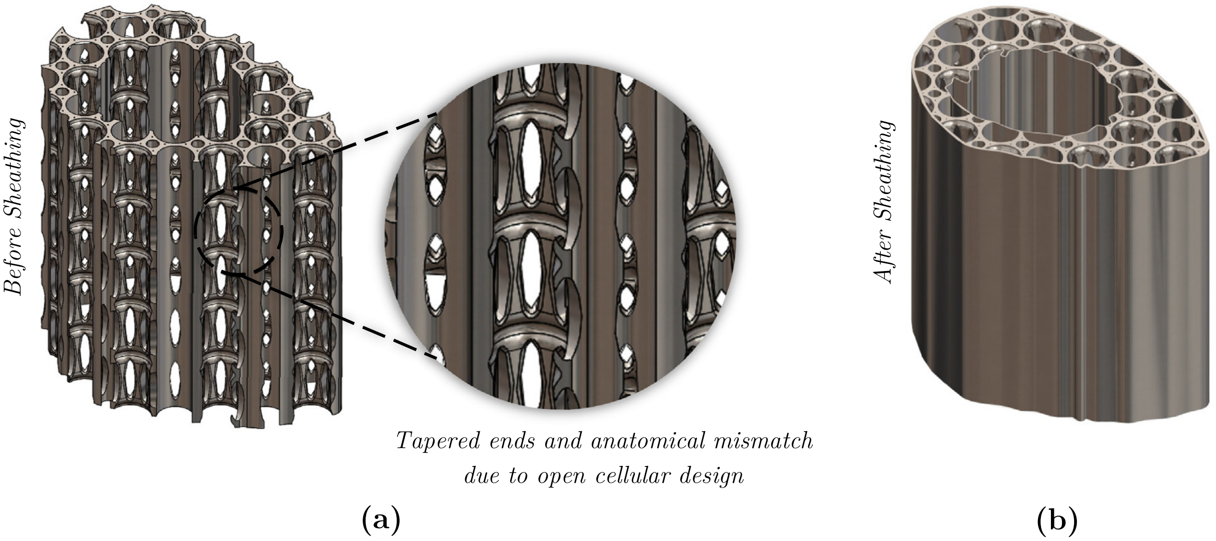

Fig. 3. SBD repair implant design based on linearly arranged unit cells showing (a) before sheathing exhibiting geometrical anomalies along with anatomical mismatch and (b) after sheathing.

Table 1
Elemental distribution and solution parameters associated with FEA.

Model reference	Max element size (mm)	Min element size (mm)	Total nodes	Total elements	Mesh time (hh:mm:ss)	Solution time (hh:mm:ss)
A1	0.25	0.05	224151	150,180	00:12:00	00:27:00
B1	0.25	0.05	508773	351,682	00:19:00	00:38:00
C1	0.25	0.05	257845	164,022	00:17:00	00:31:00
D1	0.25	0.05	524775	363,697	00:24:00	00:45:00
SBD implant	0.265	0.035	2607988	1,304,540	00:34:58	01:20:00

During the sintering process, a horizontally scanning laser beam was used fused together the Ti64 particles by melting. The process operated on a layer-by-layer technique and the build platform was lowered vertically on completion of each layer. After this, the next layer was prepared by the powder feeder and re-coater spreading the powder. After recoating, the laser induced melting is applied on the new layer and the process repeats.

Before the start of the process, the Ti64 powder was mixed for 1 h in a tumble mixer to achieve homogenous distribution. The particle size was then evaluated using a particle analyser to be ≈25–40 μm. Based on the particle size, the powder was processed at a layer thickness of 40 μm. The implant prototypes were sintered on a titanium plate of dimensions 100 × 100 × 10 mm mounted on a heating plate at 230 °C. The Ti plate was sand-blasted and cleaned with acetone before installing it into the machine. The laser power was set constantly at 195 W. The laser sintering parameters (hatch distance of 0.05 mm, 0.075 mm and 0.1 mm; laser scan speed of 7 mm/s) were combined to obtain a dense part. Before the start of the sintering process, the machine chamber was held ~20 min inactive to achieve an oxygen level of <0.2% while the base plate was heated to the set temperature.

2.5. Mechanical testing

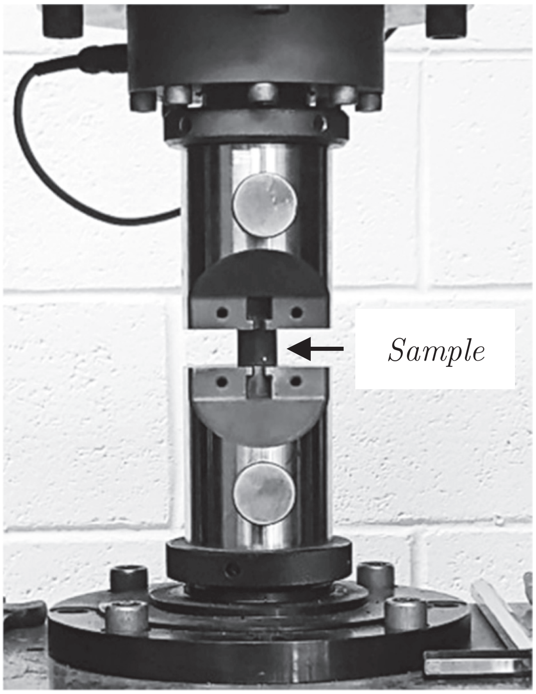

Fig. 5. Experimental compression test setup.

Compression tests were performed using a Zwick Roell Z1474 materials testing machine having a maximum load capacity of 100 kN as shown in Fig. 5. The physical tests were performed to investigate both the compressive performance of SBD implant and the tibial bone to be replaced. BS EN ISO 7500-1 [51] was referred for the calibration and verification of the test setup.

The test samples were loaded to failure through crosshead displacement at the rate of 10 N/s. A maximum load of 90 kN with a force shutdown threshold of 20% and maximum deformation of 10% were applied. The threshold and deformation values ensured that the compression plates were restrained from colliding. Realtime force-displacement and stress strain curves were obtained for further analysis.

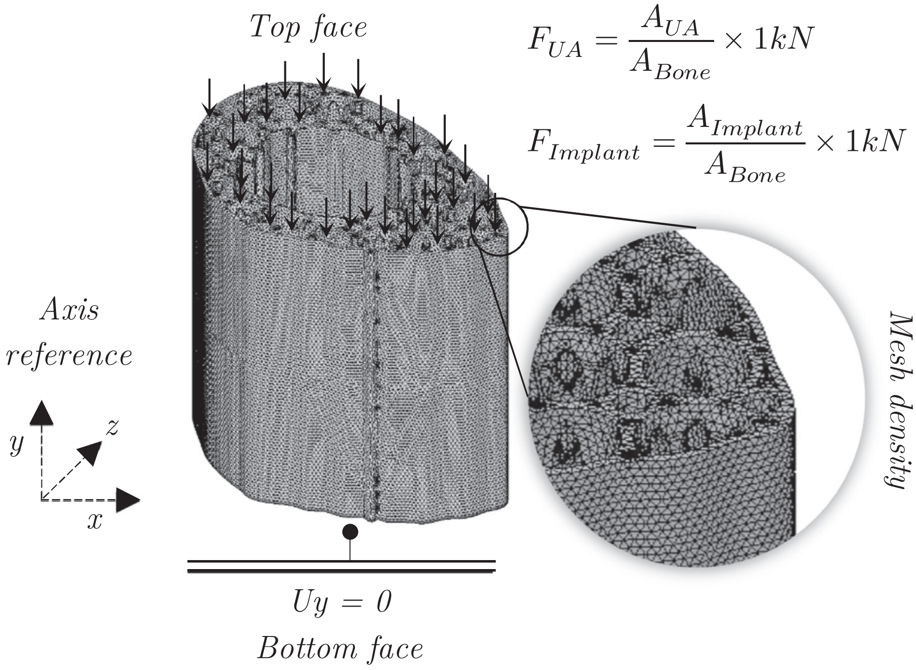

Fig. 4. Boundary condition and mesh resolution of the finite element model.

2.6. Surface roughness and microstructure characterisation

The surface roughness of the implant resulting from DMLS was evaluated using Olympus LEXT OLS3100 confocal laser scanning microscope. The laser identified the lowest site and referenced this as zero, from which peaks and valleys were referenced. The microstructure was further evaluated using a Scanning Electron Microscope (SEM) and porosity though X-ray μCT scan technique. A total of 4166 images were collected at 2.5 μm voxel size. Based on this the 3D tomogram was reconstructed from the transmission images using standard beam hardening correction and Gaussian smoothening with 0.5–0.7 kernel size with the help of NRecon (Bruker).

Furthermore, the total porosity and pore interconnectivity in the 3D reconstructed data were estimated using CTVox. For this, the reconstructed images were further processed, and an interactive thresholding and watershed segmentation were used to get a binary image, where voxels corresponding to material and pores were assigned as two different phases. The threshold values were adjusted manually to cover the entire region of interest (ROI). Subtracting the binary image of pore material from the mask, the pore volume was obtained. The scan data was visualised using a 3D volume rendering and iso-surface module.

3. Results

3.1. Unit cell selection

The four unit cells, A1, B1, C1 and D1 (Fig. 2) were analysed using both hand calculation and FEA, the results of which are summarised in Table 2. The unit cell density values were evaluated using Eq. (2); where the mass and volume were obtained from CAD. Further to this, relative density of the unit cell to the bulk material was reviewed using Eq. (3). Where, ρ_{UC} is the density of the unit cell, m_{UC} is the mass of the unit cell and $V_{B\ (UC)}$ is the volume of the bulk material.

$$\rho_{UC} = \frac{m_{UC}}{V_{B\ (UC)}} \tag{2}$$

$$\rho_{r\ (UC)} = \frac{\rho_{UC}}{\rho_B} \tag{3}$$

$$E_{(UC)} \approx E_B \cdot \rho^2_{r(UC)} \tag{4}$$

The relative Young's Modulus was then calculated using Eq. (4) where, E_B is the Young's Modulus of bulk material, $\rho_{r(UC)}$ is the relative density of the unit cell and ρ_B is the bulk material density.

The relative densities of the unit cells were comparable while exhibiting a maximum difference of 18.90% between the designs at 0.2868, 0.2326, 0.2529, 0.2461 for A1, B1, C1 and D1 respectively. While the relative density of the unit cell was a key variable for porosity, it was also crucial to analyse the associated stress distribution. Accordingly, it was considered significant to use both the stress profile and relative density for the selection of the appropriate unit cell for the implant.

Table 2
Unit cell properties from hand calculation and FEA.

Property	A1	B1	C1	D1
Unit cell mass ($m_{(UC)}$) (g)	1.270	1.030	1.120	1.090
Unit cell volume bulk ($V_{(B\text{-}UC)}$) (mm^3)	1000	1000	1000	1000
Unit cell density ($\rho_{(UC)}$) (g/mm^3)	0.0013	0.0010	0.0011	0.0011
Bulk material density ($\rho_{(B)}$) (g/mm^3)	0.0044	0.0044	0.0044	0.0044
Unit cell relative density ($\rho_{r(UC)}$)	0.2868	0.2326	0.2529	0.2461
b (number of beams)	24	24	24	24
j (number of joints)	16	16	16	16
$M = b - 3j + 6$	−18	−18	−18	−18
Bulk material Young's Modulus (E_B) (GPa)	104.80	104.80	104.80	104.80
Young's Modulus $E_{(UC)}$ (GPa)	8.62	5.67	6.70	6.35
$\Delta L_{(UC)}$ (*FEA* max) (10^{-6} m)	2.070	2.536	2.776	2.431
$\sigma_{(UC)}$ (*FEA* max) (MPa)	23.66	49.98	62.50	43.65

A three-dimensional FEA was carried out on all four unit cells and the associated von Mises stresses presented in Fig. 6. Designs A1, B1, C1 and D1 exhibited maximum von Mises stress of 23.66, 49.98, 62.50 and 43.65 MPa respectively under the same load. The lowest von Mises stress corresponded to A1 with the highest relative density 0.2868. However, the highest stress of 62.50 for unit cell C1 did not correspond to the lowest relative density. Accordingly, the influence of geometry is significant on the stress profile in comparison to the relative density. To explore this further, the stress distribution along the vertical axis of the unit cell obtained from 12 equidistant nodal probes is presented in Fig. 7.

Comparing the stress distribution shown in Fig. 7, unit cells B1 and C1 exhibited comparable performance showing distinguishable peaks and valleys dictating stress build up at areas within the structure. These designs also exhibited the first (C1) and second (B1) highest von Mises stress values out of the four designs tested. This was primarily due to design features lending to substantially uneven wall thickness at certain locations. Accordingly, these two designs were considered unsuitable as this might lead to stress concentration and catastrophic failure of the implant.

Designs A1 and D1 exhibited comparable stress distribution between locations 4 and 9. However, D1 exhibited the lowest stress gradient with von Mises stress at all locations falling within a ±4.2 MPa limit. D1 also exhibited the second lowest von Mises stress and relative density of 43.65 MPa and 0.2461 respectively. This shows that out of all the unit cells tested D1 was the most suitable for the SBD implant under consideration.

Considering a unit cell that featured even distribution of stress was also significant from a bone reintegration perspective [52]. Consequently, unit cell D1 was considered as the foundation for the SBD implant. All results from both hand calculation and FEA are summarised in Table 2.

3.2. Numerical evaluation of the implant design

The sheathed design of the SBD implant constituted to a relative density of 0.339 and structural mass of 5.72 g (rounded) with associated parameters as listed in Table 3. This resulted in a relative Young's Modulus of 12.03 GPa (E_L) based on calculations following Maxwell's criterion [53].

The FEA results obtained for the SBD sheathed implant is shown in Fig. 8. Evaluating Fig. 8a, von Mises stress distribution was even across the cellular structure. This was expected based on the performance of unit cell D1. Furthermore, no stress concentration was observed at the connection between the cells and both the internal and external sheathing. The SBD implant showed a maximum von Mises stress of 33 MPa. From Fig. 8b, the maximum deformation predicted by the finite element model is 3.551 μm. Regarding stress concentration within the cellular structure itself, the von-Mises stress between the cellular layers are almost similar and concentration was primarily at the narrowest region within the cell beams.

Based on the maximum stress and deflection from FEA, a Young's Modulus (E_{FEA}) of 11.94 GPa was obtained using Eq. (1). Comparing the Modulus obtained from FEA with predictions using Maxwell's criterion, a difference of only 0.09 GPa was found. Accordingly, the finite element results are in good agreement with the hand calculations. However, the Maxwell's criterion underestimated the Modulus of the sheathed implant by 0.75%.

The predicted E_{FEA} and E_L falls slightly below the Modulus of the cortical bone to be replaced, which was investigated experimentally to be 18.01 GPa (E_{Tibia}). In general, the Young's Modulus of cortical bone ranges between 18.6 and 20.7 GPa [13,54]. Accordingly, one of the critical aims of this study was to lower the stiffness of Ti64 implants to bring it slightly lower than the bone to be replaced in an attempt to accelerate

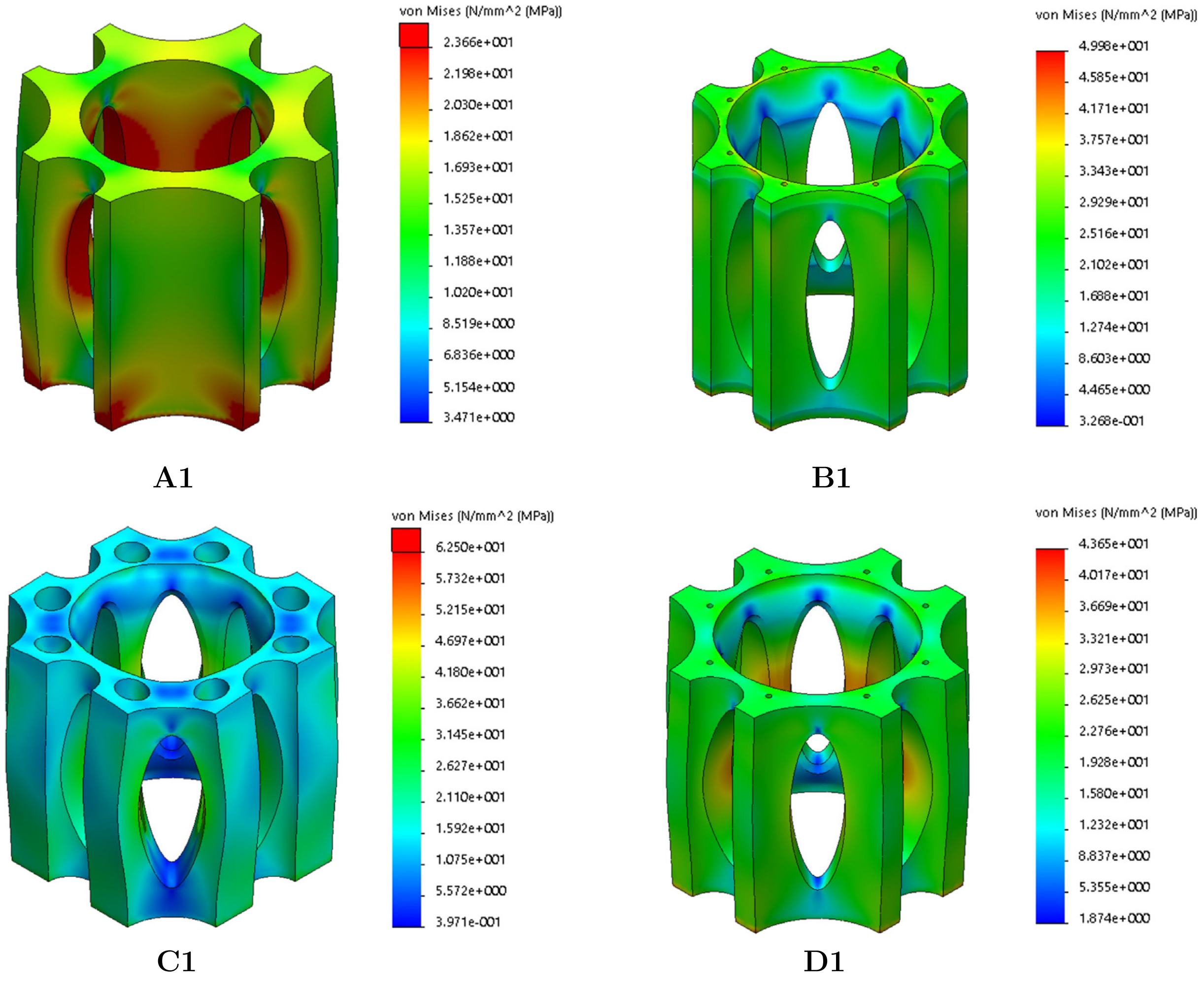

Fig. 6. Finite element stress profile of the unit cell designs under compression.

ossification. This is expected to result in a matched stiffness of the SBD implant after a period of osseointegration. However, it must be noted that the size of the implant presented here is arbitrary and osseointegration is not expected to fill the whole implant. Instead the expectation is that of a few millimetres of bone on-growth onto the rough Ti surface. Osseointegration spanning a whole defect above critical size in the absence of autologous bone graft is highly unlikely.

3.3. Manufacture and mechanical performance

Upon completion of the build, the prototype was inspected and there were no visible cracks or defects present on the outer surfaces of the implant. As expected with DMLS, a rough surface finish was created due to the stair-step effect that occurs during AM. The SBD implant was then tested using the compression testing machine to failure. The

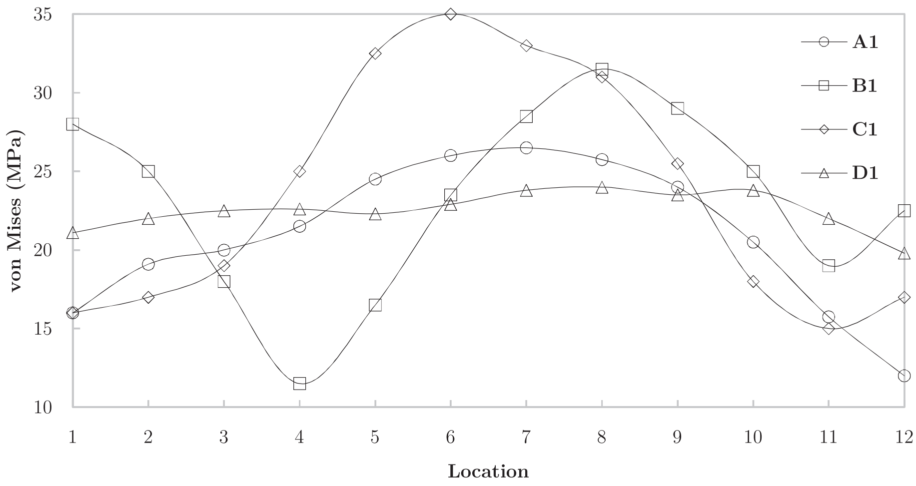

Fig. 7. Finite element nodal stress plot at 12 equidistant location along the vertical axis.

Table 3
Properties associated with the SBD implant.

Property	Sheathed implant
Mass ($M_{(L)}$) (g)	5.72
Bone bulk volume ($V_{(B-L)}$) (m^3)	3.816×10^{-6}
Density ($\rho_{(L)}$) (kg/m^3)	1500.39
Bulk material density ($\rho_{(B)}$) (kg/m^3)	4428.78
Relative density ($\rho_{(r-L)}$)	0.339
Bulk material Young's Modulus (E_B) (GPa)	104.8
Young's Modulus from Maxwell's criterion (GPa) (E_L)	12.03

implant prototype before and after the test are shown in Fig. 9a and b respectively.

On initial assessment of the failed sample shown in Fig. 9b, failure patterns resembling thin wall buckling were visible along both internal and external sheath. However, failure occurred only after an ultimate bearing strength of 0.893 GPa and 1.02 GPa for experimental test 1 (EXP1) and 2 (EXP2) respectively as shown in Fig. 10. The usual working stress that can be expected at the segmented tibial section based on a load of 100 kg for static and dynamic loading is ~5.5 and ~55.5 MPa.

In comparison, the implant being considered is far superior exhibiting a bearing strength approximately twice (EXP2) that of the dynamic working stress expected at the tibial section. However, an implant performance closer to the working stress may be beneficial to accelerate the process of ossification. Furthermore, between the experimental tests a percentage difference of 13.27% was observed on samples manufactured under similar criteria. Repeatability issues in additive manufacturing of Ti64 is a known factor and have been the subject of several studies, normally a ±15% deviation is yield strength and 5% is young's modulus is considered ‘usual’ [55–57] of the DMLS process.

The stress-strain curve from experimental test shown in Fig. 10 exhibits a typical profile that can be expected from Ti64 [58]. The test resulted in a Young's Modulus of 13.98 (E_{EXP1}) and 14.58 GPa (E_{EXP2}) based on an applied compressive load of 10.5 kN and cross-sectional area of 180.02 mm^2. Between the two tests, a difference of 4.8% was observed which shows that the elastic performance of the implant is repeatable within widely accepted range [59]. Comparing the experimental Modulus with FEA (E_{FEA}), a highest difference of 2.74 GPa was observed. Consequently, the FEA underestimated the Young's Modulus by 18.1% with respect to experimental tests (highest difference). Following similar procedure, the tests on the segmented tibial bone resulted in a Young's Modulus (E_{Tibia}) of 18.01 GPa.

The bearing strength of biocompatible Ti64 manufactured by EOS corresponding to ISO 5832-3 [60] chemical composition used for implant manufacture has a bearing strength of 1.14 GPa [49]. Comparing this to the experimentally observed value of 0.893 GPa and 1.02 GPa, difference of 0.247 and 0.12 GPa was observed respectively. This was a percentage reduction of 24.3% for EXP1 and 10.5% for EXP2 at a relative density of 33.9%. The lower E value at a relatively high bearing strength is typical of Ti64 cellular structures under compression with vertical reinforcement as reported by Campanelli et al. [58]. In comparison, the

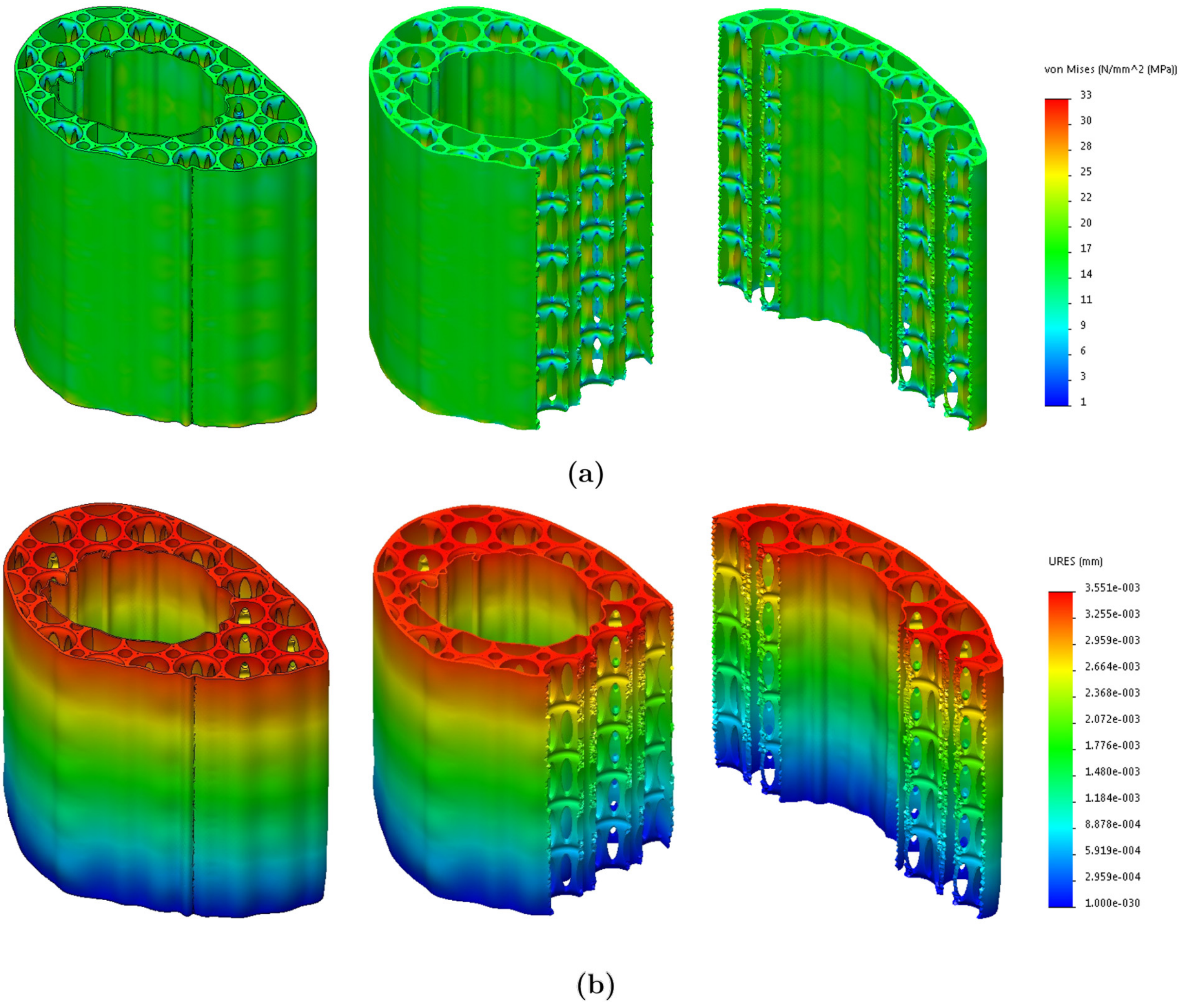

Fig. 8. von Mises stress distribution and nodal deformation obtained from FEA.

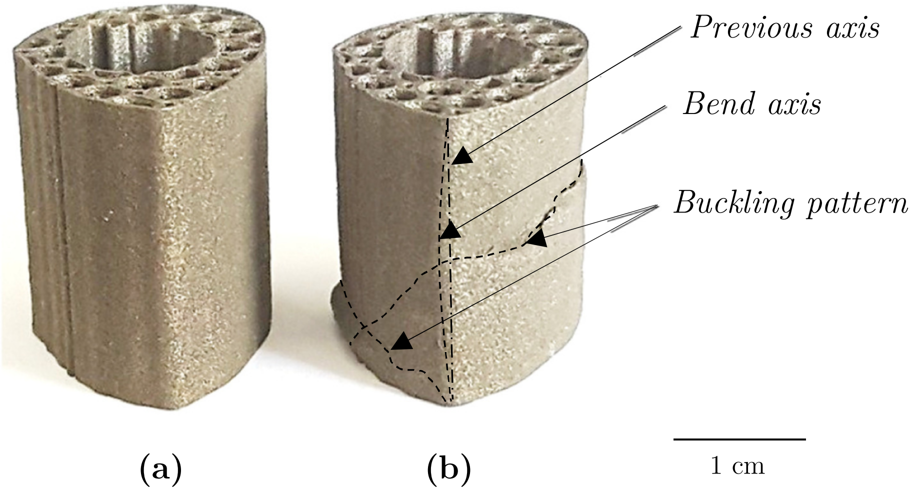

Fig. 9. DMLS implant prototypes, (a) before testing and (b) failed specimen.

sheathed design of the implant acts as vertical reinforcement significantly enhancing the bearing strength. Furthermore, the uniform stress distribution within the adopted unit cell (D1) means that the strain is equally distributed resulting in a lower modulus.

3.4. Surface roughness and microstructure

Three-dimensional surface interrogation of the DMLS implant using Confocal Laser Scanning Microscopy (CLSM) revealed a non-perfect surface with peaks and valleys typical of a Ti64 DMLS sample as shown in Fig. 11a–b. The surface morphology of the implant at 160 μm is presented in Fig. 11b, where sintered titanium powder is visible; ranging between fully melted compositions to partially sintered at approximately 40 μm diameter.

It is evident that the semi-melted powder particles adhering to the surface was the cause of the rough surface finish. Furthermore, laser strip marks typical of the AM process is visible on all fully melted surfaces. A sampling of 960 μm square was considered for analysis and the surface roughness profile was evaluated to be between 25 μm and 90 μm with a mean value of 56.78 μm as shown in Fig. 11c. While the surface roughness aspect of the implant enabled to characterise the manufacturing quality from the DMLS standpoint, further evaluation is necessary in terms biomechanical performance, cytotoxicity and long-term biocompatibility which was not considered in this study. Consequently, systematic analysis following ISO 10993-5 [61] for the design and manufacture of metallic bone implants and fixation is necessary before practical application is possible.

The microporosity of the DMLS implant depends on powder morphology as well as process parameters and hence is expected to be same for all the samples manufactured. The estimation of porosity using micro-CT was limited by the 'voxel size' [62] of 2.5 μm making pores smaller than the 'voxel size' out of range recognised as fully dense. From Fig. 12, it is evident that the microporosity is homogenously across the implant. Furthermore, the number of the independent pores was found to be >2 vol% resulting in 98% interconnected microporosity.

This extent of interconnectivity in micropores is extremely relevant in the context of vascularisation and neoangiogenesis, which helps in transport of nutrients, biological cues, and oxygen to tissues and removal of metabolic wastes [63]. Furthermore, Fig. 12b shows that the lattice structures feature homogenous microporosity and are not expected to fail locally due to density gradation. Based on the 3D reconstructed volume of μCT data using CTVox (volume rendering) package the volumetric porosity was evaluated as 64.5%. In comparison to the CAD based porosity of 66.1%, this is a difference of 1.6%. This is due to the variation in the ideal geometric surface due to the sintering process clearly observed from the magnified surface data presented in Fig. 12b.

Fig. 13b shows microcracks throughout the surface that should be considered life shortening characteristics. Previous research has

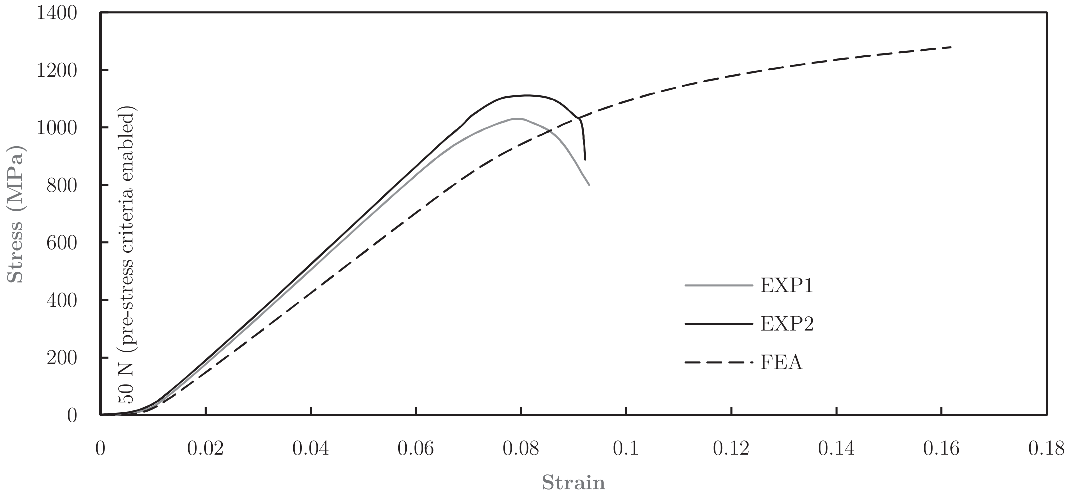

Fig. 10. Experimental stress-strain relationship for the SBD sheathed implant.

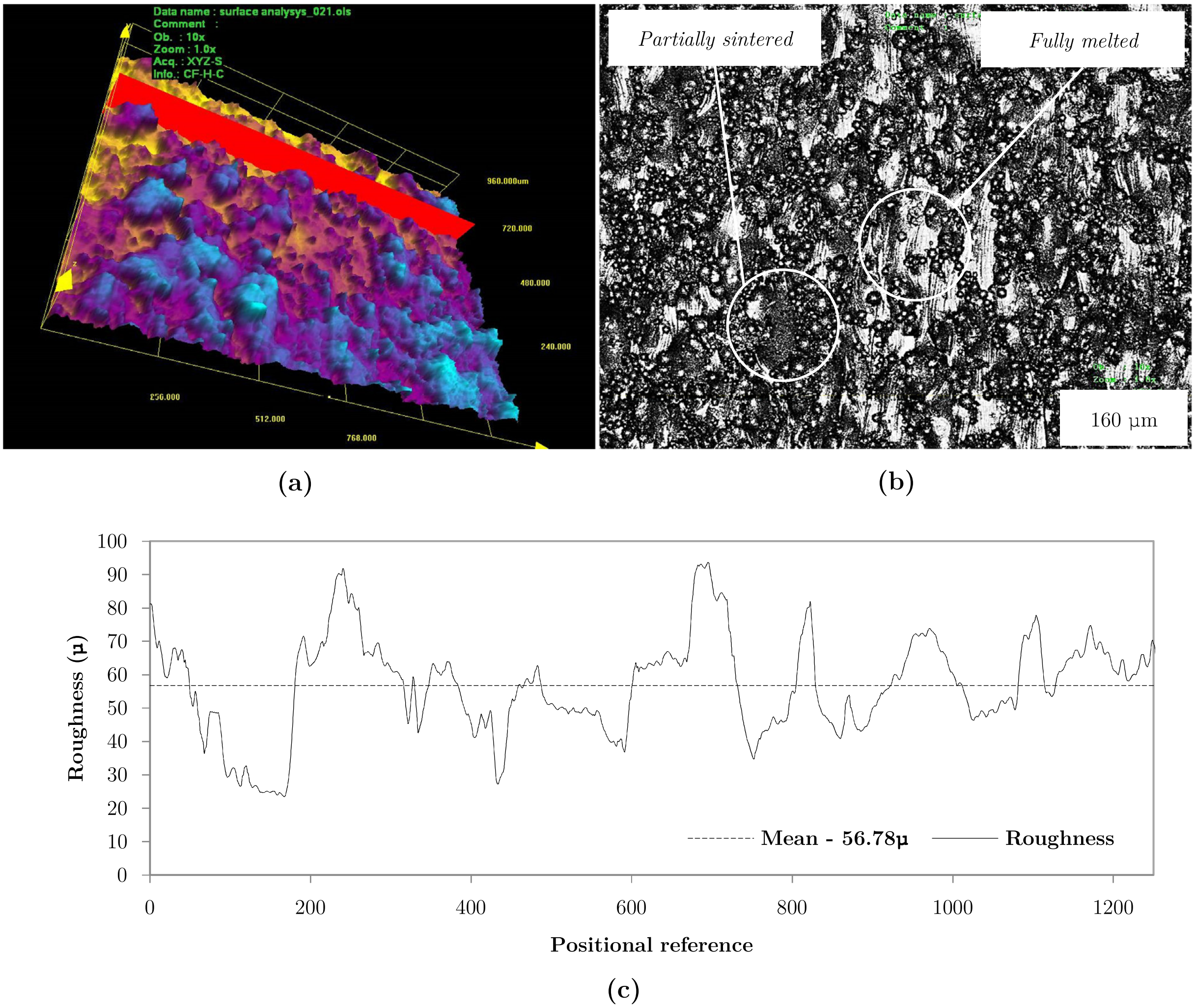

Fig. 11. Micrograph of Ti64 DMLS implant showing (a) three-dimensional roughness profile, (b) surface morphology (c) mean surface evaluation.

established that epitaxial grain growth and consequently columnar grains is the common mechanism in most of the titanium alloys such as Ti64 [66,67]. However, in various DLMS parts, different morphologies of prior beta grains were reported in near-alpha, $\alpha+\beta$, and near $-\beta$ titanium alloys. While suitable stress relief would limit the occurrence micro cracking to maintain dimensional accuracy the thermal history and build orientation must be carefully considered to identify the effects of grain growth.

4. Discussion

This work has investigated the compression behaviour of Ti64 sheathed SBD tibial implant manufactured using DMLS that closely matches the anatomy of the segmented bone featuring a functional cellular design methodology. From reviewing the literature, this is the first study to investigate the design, manufacture and performance of such an implant. It was hypothesised that the design and manufacturing approach employed in this work could provide SBD implant that exhibit stiffness matching characteristics to the host bone. While length of the implant presented is purely arbitrary, it is anticipate that a 'limited contact locking compression plate' fixing mechanism resembling the ones reported by Wieding et al. [68] and Reichert et al. [22] may be adopted as the fixing mechanism of choice. However, further studies on the whole assembly is required to evaluate the impact of such a fixing mechanism on the implant which was outside the scope of this preliminary study.

It was clear from the anatomy of the segmented bone under consideration (Fig. 1b) that it is naturally graded and porous. The advancement in CT scan technologies and integration of CAD prompted the research question whether a cellular design approach could be combined with anatomical grading to produce stiffness matching SBD implants for effective tissue regeneration. Consequently, fabricating a SBD implant to naturally mimic the anatomy using a digital bio-model (Fig. 1c) derived from X-Ray CT Scan data was the chosen approach of this study.

Stress shielding inhibits ossification, as such constant stress distribution through both unit cell and cellular structure was sought to facilitate bone growth. Further effect includes loss of already present bone because it is no longer loaded. For this reason, there is a high risk of Ti64 implant failure after about a decade of implantation. To facilitate constant stress distribution, a suitable unit cell design that can provide an even stress distribution was required. Consequently, unit cells A1, B1, C1 and D1 (Fig. 2) were considered and numerically evaluated using FEA. Comparing the results as shown in Fig. 7, D1 exhibited the lowest stress gradient. von Mises stress at all locations where comparable within a limit of ±4.2 MPa. This design also exhibited the second lowest maximum von Mises stress and relative density of 43.65 MPa (Fig. 6) and 0.2461 (Table 2) respectively. Therefore, D1 was used as the foundation for the cellular architecture for the SBD implant.

Even though initial consideration was to study both a sheathed and unsheathed design, it was deemed most suitable to pursue a sheathed design shown in Fig. 3b. This was based on the safety critical aspects

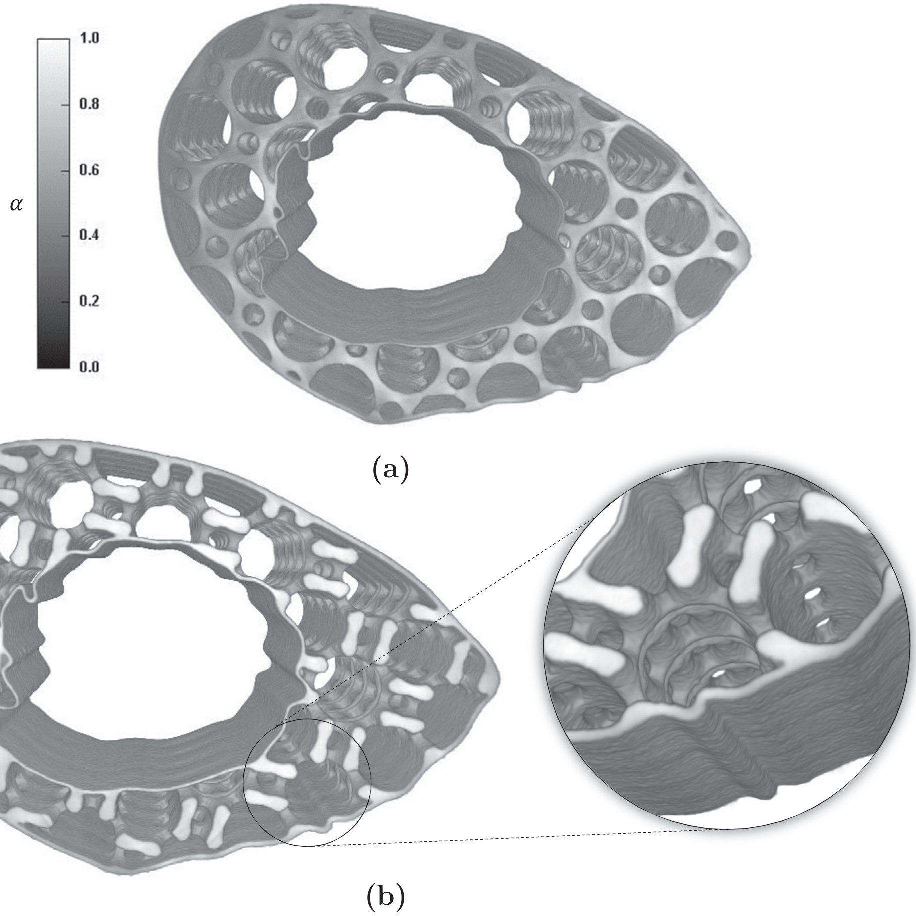

Fig. 12. Reconstructed μCT data of the sheathed implant weighted against an arbitrary opacity scale showing microporosity based on X-ray absorption (α) where 0.0–fully porous and 1.0–fully dense; where (a) top surface and (b) cross-section.

of tapered junctions that is often a feature in open cell anatomical designs as shown in Fig. 3a. Metal debris can be released from the tapered junction in open pore designs that can cause adverse soft tissue reactions in the human body [47]. While Ti64 implants are routinely used for bone fractures as well as dental work [69]. They have been shown to both corrode and degrade, generating metallic debris [70]. Accordingly, concerns are mounting over the concentrations of circulating metal debris derived from these implants, and their harmful biological effects including hepatic injury and renal lesions [71].

According to works of Nuevo-Ordóñez et al. [72], the concentration of titanium in bloodstream were significantly higher for patients with implants compared to control individuals. Furthermore, it was shown that this difference can be associated to the fixation and the invasive nature of the implants. Furthermore, certain implants were found to shed

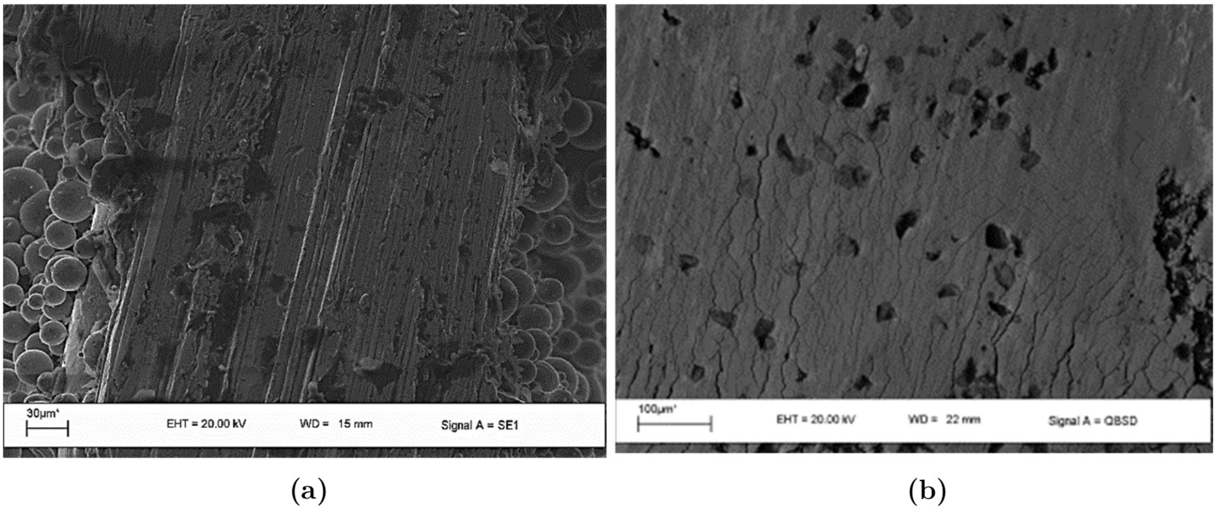

Fig. 13. Scanning electron microscope inspection showing (a) semi-melted particles on the surface (b) interfacial micro structure and cracks.

more metallic debris into the blood than the other designs. While the exact nature of the design parameters that contribute to the shedding of debris is now known, it may be beneficial to avoid tapered ends as they are susceptible to failure.

Ti64 is also known to have low wear and shear strength despite having a high Young's modulus [73,74] that need further consideration from a design perspective. Furthermore, the alloying component vanadium present in Ti64 exhibits a high cytotoxicity and aluminium may even induce senile dementia [75,76]. Accordingly, these leachable ions can cause a number of health issues such as allergic, cytotoxic effect and even neurological disorders. As implant once installed are present in the body for a long time, health problems, such as Alzheimer diseases, osteomalacia and peripheral neuropathy are also further risks worth considering for at the time of design and material selection [69].

Considering some of these health risks, despite minimising taper ends a sheathed design was also favourable to closely mimic both the interior and exterior topological anatomy of the segmented bone. Furthermore, consideration was given to the DMLS manufacturing process, which require unviable support structures in the case of an open pore anatomical structure. However, the sheathed implant design featuring cellular porosity may have a high likelihood of developing infection in the event where the porous space is not invaded by bone as it will be filled with avascular fluid [77]. Upon implantation, the implanted material is in contact with complex host bodily fluids. While, the exact nature of these fluids is patient and implant site dependent [78], blood serum is present in most tissues of the body and contains a diverse array of proteins; including complement and immunoglobulins, key mediators of early immune responses. Accordingly, further studies regarding this aspect are required before such a design can be applied for SBD repair.

The numerical analysis of the implant (Fig. 8) resulted in a Young's Modulus of 11.94 GPa. In comparison, the Maxwell's criterion underestimated the Modulus (12.03 GPa) of the sheathed implant by 0.75% (Table 3). Consequently, the Maxwell's criterion fits well with the chosen sheathed implant considered in this study. Evaluating the stress contours as shown in Fig. 8a, no stress concentration was observed at the connection between the cellular structure and both the internal and external sheathing. The SBD implant exhibited a maximum von Mises stress of 33 MPa at a maximum deformation of 3.551 μm (Fig. 8b). In comparison, the experimentally obtained stress-strain curve (Fig. 10) resulted in a Young's Modulus of 14.58 GPa; a difference of 18.1% compared to FEA.

The numerical model of the SBD implant was modelled using the volume representing the cellular structure and sheath as a continuum part featuring a single Young's Modulus. Published studies that have followed similar approach have highlighted that the stiffness can differ by up to four times in comparison with experimental test data [46,50,79]. Consequently, it can be considered that the 18.1% difference between FEA and experimental allows for a reasonable agreement. This shows that SBD anatomical implants under compression can be modelled with reasonable accuracy using the finite element methodology presented in this study. Furthermore, the mixed mesh featuring the mid-node shell element can contribute towards reducing the size of the elemental matrix and hence computational cost.

As listed in Table 4, the Young's Modulus of the SBD implant developed in this study was slightly lower than Modulus of the segmented bone to be replaced. While the segmented tibial bone exhibited a Young's Modulus of 18.01 GPa, the implant showed 14.58 GPa. In general, the Young's Modulus of cortical bone range between 18.6 and 20.7 GPa [8,37]. The critical aim of the study was to lower the stiffness of Ti64 SBD implants to bring it slightly below to that of the bone in an attempt to accelerate ossification. This is expected to result in a matched stiffness of the SBD implant after a period of osseointegration. Accordingly, this study presents a design methodology that can substantially lower the stiffness of Ti64 implants to bring it closer to the bone to be replaced.

Table 4
Young's Modulus of the SBD repair implant and that of the bone to be replaced.

Ti64 SBD implant			Bone
E_L	E_{FEA}	E_{EXP}	E_{Tibia}
12.03 GPa	11.94 GPa	14.58 GPa	18.01 GPa

Evaluating the deformed test specimen (Fig. 9b), the primary failure mode appears to be buckling. The approximated radial buckling occurred at 61.5 mm measured at the planar centre. This is the result of non-uniform stress induced in the sheath due to the anatomical geometry. However, the implant started yielding only at 1.02 GPa (Fig. 10) in comparison to a dynamic working stress of ~55.5 MPa for the tibial section. Therefore, the implant is structurally superior and safe from a practical point of view, capable of accommodating approximately twice the dynamic stress that can be expected. A further reduction in the bearing strength of the implant to make it perform closer to the working stress of the tibia may be beneficial to accelerate ossification. However, compared to the bearing strength of Ti64 DMLS powder [49], the implant showed a reduction in performance by 10.5% at a relative density of 33.9%.

Inspections using CLSM revealed a surface typical of a Ti64 DMLS sample, where Ti particles ranged between fully melted compositions to partially sintered at approximately 40 μm diameter where present (Fig. 11b). This resulted in a mean roughness of 56.78 μm. The semi-fused particles that adhered to the surface (Fig. 13) is likely due to melt-pool turbulence and particle energy volatility. From the works of Bonfield [80], a pore size and surface roughness approximately 50 μm (diameter) and 40 μm respectively can accommodate osteoblasts efficiently. Furthermore, Precursor osteoblasts that are of interest to this study, are around 10 μm which can cling on to the presented surface effectively. However, osteoblasts can be found in various sizes and once mature osteoblast can be over 200 μm. Taniguchi et al. [81] studied DMLS Ti cellular structures at a porosity of 60%, with respect to cancellous bone ingrowth, in vivo. The results showed that for ingrowth, pores around 600 μm and 400 μm performed best and worst respectively. In comparison, the SBD repair implant presented in this study represents a porosity value of 64.5% and an average pore size of 723 μm, consequently further evaluation is required to quantify the extend of potential bone growth.

The key challenge in this study was to tailor the desirable mechanical properties of the implant to minimise failure by stiffness matching. Bulk titanium exceeds the Young's Modulus of cortical bone by more than three-fold resulting in stress shielding and subsequent weakening of the connection between the bone and the implant. However, the presented Ti64 implant performs slightly lower than the Modulus of the segmented bone for stiffness matching after a period of bone ingrowth. Furthermore, the cellular structure porosity and the surface roughness resulted from the DMLS process can enhance osteogenesis. This work has proposed and validated a methodology using X-Ray CT Scan, DMLS and FEA to develop a porous sheathed anatomical SBD implant that could potentially assist in reducing stress shielding and thereby improving the longevity of Ti64 implants.

4.1. Limitations and future work

The overall dimensions of SBD repair presented in this study is arbitrary and is not representative of a practical scenario. For dimensions above the critical length autologous grafts need to be considered for effective osteointegration [23]. Consequently, the results presented in this study are limited to the primary understanding of the compression behaviour of a potential anatomical implant where the methodology may be adopted for stiffness-matching. Furthermore, the scope of this study is limited to the mechanical behaviour, omitting any thermal or flow characterisation. Nevertheless, the flow characterisation of the implant along with in vitro tests of cytotoxicity and then mesenchymal stem cell and/or osteoblast attachment will be considered as part of future work.

5. Conclusions

This research presents the design, development and manufacture of a porous Ti64 SBD repair implant that anatomically mimics the segmented bone of the tibial section. The global implant design was based on the sectional anatomy captured using X-ray Computed Tomography. The implant has an internal porosity of 64.5% while featuring a suitable cellular structure. The resulting Young's Modulus for the implant were 12.03, 11.94 and 14.58 GPa using Maxwell's criterion, FEA and physical tests (EXP2) respectively. This was slightly lower than the segmented bone that exhibited 18.01 GPa to allow for stiffness matching to occur following a period of osseointegration. Good correlation was achieved between the numerical and experimental data indicating that the simplified finite element methodology presented in this study is suitable for modelling the behaviour of porous anatomical implants undergoing compression. The DMLS manufacturing process was found to contribute to a favourable surface roughness of 56.78 μm, which is constructive for osteogenesis. It is anticipated that the cellular design methodology proposed in this study can aid the development of functional anatomical SBD implants that can reduce stress shielding by allowing for stiffness matching after a period of bone ingrowth. However, in-vitro incubation using bio-reactors in necessary to quantify actual bone ingrowth within the implant under dynamic loading.

CRediT authorship contribution statement

Aaron Vance: Methodology, Formal analysis, Investigation. **Klaudio Bari:** Conceptualization, Investigation. **Arun Arjunan:** Writing - original draft, Writing - review & editing, Visualization, Validation, Formal analysis.

Acknowledgements

This research was supported by both the University of Derby and University of Wolverhampton. The bone samples used in this study were provided by Dr. Graham Souch.

Data availability

The data that support the findings of this study are available from the corresponding author upon reasonable request.

References

[1] R. Chung, D.M. Kalyon, X. Yu, A. Valdevit, Segmental bone replacement via patient-specific, 3D printed bioresorbable graft substitutes and their use as templates for culture of mesenchymal stem cells under mechanical stimulation at various frequencies, Biotechnol. Bioeng. 25 (Jun 2018).
[2] K.B. Hazlehurst, C.J. Wang, M. Stanford, An investigation into the flexural characteristics of functionally graded cobalt chrome femoral stems manufactured using selective laser melting, Mater. Des. 60 (Aug 2014) 177–183.
[3] S. Berretta, K. Evans, O. Ghita, Additive manufacture of PEEK cranial implants: manufacturing considerations versus accuracy and mechanical performance, Mater. Des. 139 (Feb 5, 2018) 141–152.
[4] E. Chicardi, C.F. Gutiérrez-González, M.J. Sayagués, C. García-Garrido, Development of a novel TiNbTa material potentially suitable for bone replacement implants, Mater. Des. 145 (May 5, 2018) 88–96.
[5] S.M. Ahmadi, R. Hedayati, Y. Li, K. Lietaert, N. Tümer, A. Fatemi, et al., Fatigue performance of additively manufactured meta-biomaterials: the effects of topology and material type, Acta Biomater. 65 (2018) 292–304.
[6] R.D. Carpenter, B.S. Klosterhoff, F.B. Torstrick, K.T. Foley, J.K. Burkus, C.S.D. Lee, et al., Effect of porous orthopaedic implant material and structure on load sharing with simulated bone ingrowth: a finite element analysis comparing titanium and PEEK, J. Mech. Behav. Biomed. Mater. 80 (2018) 68–76.
[7] Y. Chen, J.E. Frith, A. Dehghan-Manshadi, H. Attar, D. Kent, N.D.M. Soro, et al., Mechanical properties and biocompatibility of porous titanium scaffolds for bone tissue engineering, J. Mech. Behav. Biomed. Mater. 75 (Nov 2017) 169–174.
[8] S. Arabnejad, B. Johnston, M. Tanzer, D. Pasini, Fully porous 3D printed titanium femoral stem to reduce stress-shielding following total hip arthroplasty, J. Orthop. Res. 35 (8) (Aug 2017) 1774–1783.
[9] A.S.M. Croitoru, B.A. Pacioga, C.S. Comsa, Personalized hip implants manufacturing and testing, Appl. Surf. Sci. 417 (Sep 30, 2017) 256–261.
[10] Noyama Yoshihiro, Miura Takuya, Ishimoto Takuya, Itaya Takahiro, Niinomi Mitsuo, Nakano Takayoshi, Bone loss and reduced bone quality of the human femur after total hip arthroplasty under stress-shielding effects by titanium-based implant, Mater. Trans. 53 (3) (2012) 565–570.
[11] R. Huiskes, H. Weinans, B. Rietbergen, The relationship between stress shielding and bone resorption around total hip stems and the effects of flexible materials, Clin. Orthop. Relat. Res. 274 (Jan 1, 1992) 124–134.
[12] Z. Yao, T. Lin, J. Pajarinen, T. Sato, S. Goodman, Chapter 12 - host response to orthopedic implants (metals and plastics), Host Response to Biomaterials, Elsevier Inc 2015, pp. 315–373.
[13] Y. Torres, P. Trueba, J.J. Pavón, E. Chicardi, P. Kamm, F. García-Moreno, et al., Design, processing and characterization of titanium with radial graded porosity for bone implants, Mater. Des. 110 (Nov 15, 2016) 179–187.
[14] M.I.Z. Ridzwan, S. Shuib, A.Y. Hassan, A.A. Shokri, M.N. Mohamad Ibrahim, Problem of stress shielding and improvement to the hip implant designs: a review, J. Med. Sci. 7 (2007) 460–467.
[15] A. Ataee, Y. Li, D. Fraser, G. Song, C. Wen, Anisotropic Ti-6Al-4V gyroid scaffolds manufactured by electron beam melting (EBM) for bone implant applications, Mater. Des. 137 (Jan 5, 2018) 345–354.
[16] L. Wang, J. Kang, C. Sun, D. Li, Y. Cao, Z. Jin, Mapping porous microstructures to yield desired mechanical properties for application in 3D printed bone scaffolds and orthopaedic implants, Mater. Des. 133 (Nov 5, 2017) 62–68.
[17] D.W. Hutmacher, Scaffolds in tissue engineering bone and cartilage, Biomaterials 21 (24) (2000) 2529–2543.
[18] M. Tarik Arafat, I. Gibson, X. Li, State of the art and future direction of additive manufactured scaffolds-based bone tissue engineering, Rapid Prototyp. J. 20 (1) (Jan 14, 2014) 13–26.
[19] Q. Ye, G. He, In-situ formed graded microporous structure in titanium alloys and its effect on the mechanical properties, Mater. Des. 83 (Oct 15, 2015) 295–300.
[20] S. Bose, S. Vahabzadeh, A. Bandyopadhyay, Bone tissue engineering using 3D printing, Mater. Today 16 (12) (Dec 2013) 496–504.
[21] F.E. Wiria, J.Y.M. Shyan, P.N. Lim, F.G.C. Wen, J.F. Yeo, T. Cao, Printing of titanium implant prototype, Mater. Des. 31 (2010) S105.
[22] J. Reichert, M. Wullschleger, A. Cipitria, J. Lienau, T. Cheng, M. Schütz, et al., Custom-made composite scaffolds for segmental defect repair in long bones, Int. Orthop. 35 (8) (Aug 2011) 1229–1236.
[23] J.P. Schmitz, J.O. Hollinger, The critical size defect as an experimental model for craniomandibulofacial nonunions, Clin. Orthop. Relat. Res. 205 (Apr 1986) 299–308.
[24] J.O. Hollinger, J.C. Kleinschmidt, The critical size defect as an experimental model to test bone repair materials, J. Craniofac. Surg. 1 (1) (Jan 1990) 60–68.
[25] H. Pape, A. Evans, P. Kobbe, Autologous bone graft: properties and techniques, J. Orthop. Trauma 24 (Suppl. 1) (Mar 2010) (Supplement:S40).
[26] F. Eckstein, M. Hudelmaier, R. Putz, The effects of exercise on human articular cartilage, J. Anat. 208 (4) (Apr 2006) 491–512.
[27] C. Ding, G. Jones, A. Wluka, F. Cicuttini, What can we learn about osteoarthritis by studying a healthy person against a person with early onset of disease? Curr. Opin. Rheumatol. 22 (5) (Sep 2010) 520–527.
[28] B. Antony, A. Venn, F. Cicuttini, L. March, L. Blizzard, T. Dwyer, et al., Association of physical activity and physical performance with tibial cartilage volume and bone area in young adults, Arthritis Res. Ther. 17 (2015) 298.
[29] M. Nilsson, D. Sundh, C. Ohlsson, M. Karlsson, D. Mellström, M. Lorentzon, Exercise during growth and young adulthood is independently associated with cortical bone size and strength in old Swedish men, J. Bone Miner. Res. 29 (8) (Aug 2014) 1795–1804.
[30] H. Attar, S. Ehtemam-Haghighi, D. Kent, M.S. Dargusch, Recent developments and opportunities in additive manufacturing of titanium-based matrix composites: a review, Int. J. Mach. Tools Manuf. 133 (Oct 2018) 85–102.
[31] D.D. Lima, S.A. Mantri, C.V. Mikler, R. Contieri, C.J. Yannetta, K.N. Campo, et al., Laser additive processing of a functionally graded internal fracture fixation plate, Mater. Des. 130 (Sep 15, 2017) 8–15.
[32] M. Dumas, P. Terriault, V. Brailovski, Modelling and characterization of a porosity graded lattice structure for additively manufactured biomaterials, Mater. Des. 121 (May 5, 2017) 383–392.
[33] J.J. de Damborenea, M.A. Larosa, M.A. Arenas, J.M. Hernández-López, A.L. Jardini, M.C.F. Ierardi, et al., Functionalization of Ti6Al4V scaffolds produced by direct metal laser for biomedical applications, Mater. Des. 83 (Oct 15, 2015) 6–13.
[34] K. Bari, C. Osarinmwian, E. López-Honorato, T.J. Abram, Characterization of the porosity in TRISO coated fuel particles and its effect on the relative thermal diffusivity, Nucl. Eng. Des. 265 (2013) 668–674.
[35] Rafael Ferreira Gregolin, Cecília Amelia de Carvalho Zavaglia, Ruís Camargo Tokimatsu, João A. Pereira, Biomechanical stress and strain analysis of mandibular human region from computed tomography to custom implant development, Adv. Mater. Sci. Eng. (Jan 1, 2017) 2017.
[36] D. Kytýř, P. Zlámal, P. Koudelka, T. Fíla, N. Krčmářová, I. Kumpová, et al., Deformation analysis of gellan-gum based bone scaffold using on-the-fly tomography, Mater. Des. 134 (Nov 15, 2017) 400–417.
[37] M.A. Surmeneva, R.A. Surmenev, E.A. Chudinova, A. Koptioug, M.S. Tkachev, S.N. Gorodzha, et al., Fabrication of multiple-layered gradient cellular metal scaffold via electron beam melting for segmental bone reconstruction, Mater. Des. 133 (Nov 5, 2017) 195–204.

[38] S. Limmahakhun, A. Oloyede, K. Sitthiseripratip, Y. Xiao, C. Yan, Stiffness and strength tailoring of cobalt chromium graded cellular structures for stress-shielding reduction, Mater. Des. 114 (Jan 15, 2017) 633–641.

[39] Xiaojian Wang, Shanqing Xu, Shiwei Zhou, Wei Xu, Martin Leary, Peter Choong, M. Qian, Milan Brandt, Yi Min Xie, Topological design and additive manufacturing of porous metals for bone scaffolds and orthopaedic implants: a review, Biomaterials 83 (2016) 127–141.

[40] S. Lohfeld, S. Cahill, H. Doyle, P. McHugh, Improving the finite element model accuracy of tissue engineering scaffolds produced by selective laser sintering, J. Mater. Sci. Mater. Med. 26 (1) (Jan 2015) 1–12.

[41] G. Campoli, M.S. Borleffs, S. Amin Yavari, R. Wauthle, H. Weinans, A.A. Zadpoor, Mechanical properties of open-cell metallic biomaterials manufactured using additive manufacturing, Mater. Des. 49 (Aug 2013) 957–965.

[42] Y. Chen, T. Li, Z. Jia, F. Scarpa, C. Yao, L. Wang, 3D printed hierarchical honeycombs with shape integrity under large compressive deformations, Mater. Des. 137 (Jan 5, 2018) 226–234.

[43] Y. Chen, Z. Jia, L. Wang, Hierarchical honeycomb lattice metamaterials with improved thermal resistance and mechanical properties, Compos. Struct. 152 (2016) 395–402.

[44] H. Yin, X. Huang, F. Scarpa, G. Wen, Y. Chen, C. Zhang, In-plane crashworthiness of bio-inspired hierarchical honeycombs, Compos. Struct. 192 (May 15, 2018) 516–527.

[45] H. Attar, M. Calin, L.C. Zhang, S. Scudino, J. Eckert, Manufacture by selective laser melting and mechanical behavior of commercially pure titanium, Mater. Sci. Eng. A 593 (Jan 21, 2014) 170–177.

[46] J. Parthasarathy, B. Starly, S. Raman, A design for the additive manufacture of functionally graded porous structures with tailored mechanical properties for biomedical applications, J. Manuf. Process. 13 (2) (2011) 160–170.

[47] D.J. Langton, R. Sidaginamale, J.K. Lord, A.V.F. Nargol, T.J. Joyce, Taper junction failure in large-diameter metal-on-metal bearings, Bone Joint Res. 1 (4) (Apr 2012) 56–63.

[48] W.G. Shadid, A. Willis, Bone fragment segmentation from 3D CT imagery, Comput. Med. Imaging Graph. 66 (2018) 14–27.

[49] Robert Stirling, EOS Titanium Ti64 Material Data Sheet, Available at: http://www.crpm.co.za/wp-content/uploads/2017/07/M280-Titanium_Material_data_sheet_10-11_en.pdf 2017.

[50] K. Hazlehurst, C.J. Wang, M. Stanford, Evaluation of the stiffness characteristics of square pore CoCrMo cellular structures manufactured using laser melting technology for potential orthopaedic applications, Mater. Des. 51 (Oct 2013) 949–955.

[51] BS EN ISO 7500-1:2018, Metallic Materials. Calibration and Verification of Static Uniaxial Testing Machines. Tension/compression Testing Machines. Calibration and Verification of the Force-measuring System, Mar 22, 2018.

[52] E. Seeman, P.D. Delmas, Bone quality – the material and structural basis of bone strength and fragility, N. Engl. J. Med. 354 (21) (May 25, 2006) 2250–2261.

[53] M.F. Ashby, The properties of foams and lattices, Philos. Trans. R. Soc. A Math. Phys. Eng. Sci. 364 (1838) (Jan 15, 2006) 15–30.

[54] J.Y. Rho, R.B. Ashman, C.H. Turner, Young's modulus of trabecular and cortical bone material: ultrasonic and microtensile measurements, J. Biomech. 26 (2) (1993) 111–119.

[55] Q. Feng, Q. Tang, Y. Liu, R. Setchi, S. Soe, S. Ma, et al., Quasi-static analysis of mechanical properties of Ti6Al4V lattice structures manufactured using selective laser melting, Int. J. Adv. Manuf. Technol. 94 (5) (Feb 2018) 2301–2313.

[56] Hernández D. García, Mechanical Behaviour Assessment of the Ti6Al4V Alloy Obtained by Additive Manufacturing Towards Aeronautical Industry, 2014 (Thesis).

[57] R. Wauthle, B. Vrancken, B. Beynaerts, K. Jorissen, J. Schrooten, J. Kruth, et al., Effects of build orientation and heat treatment on the microstructure and mechanical properties of selective laser melted Ti6Al4V lattice structures, Addit. Manuf. 5 (Jan 2015) 77–84.

[58] Sabina L. Campanelli, Nicola Contuzzi, Antonio D. Ludovico, Fabrizia Caiazzo, Francesco Cardaropoli, Vincenzo Sergi, Manufacturing and characterization of Ti6Al4V lattice components manufactured by selective laser melting, Materials 7 (6) (Jun 1, 2014) 4803–4822.

[59] M. Mazur, M. Leary, S. Sun, M. Vcelka, D. Shidid, M. Brandt, Deformation and failure behaviour of Ti-6Al-4V lattice structures manufactured by selective laser melting (SLM), Int. J. Adv. Manuf. Technol. 84 (5) (May 2016) 1391–1411.

[60] Implants for Surgery - Metallic Materials - Part 3: Wrought Titanium 6-Aluminium 4-vanadium Alloy (ISO 5832-3:2016)Feb 1, 2017.

[61] ISO, ISO 10993-5:2009: Biological Evaluation of Medical Devices – Part 5: Tests for In Vitro Cytotoxicity, International Organization for Standardization, 2009.

[62] D. Maret, N. Telmon, O.A. Peters, B. Lepage, J. Treil, J.M. Inglèse, et al., Effect of voxel size on the accuracy of 3D reconstructions with cone beam CT, Dentomaxillofac. Radiol. 41 (8) (Dec 2012) 649–655.

[63] S. Barui, S. Chatterjee, S. Mandal, A. Kumar, B. Basu, Microstructure and compression properties of 3D powder printed Ti-6Al-4V scaffolds with designed porosity: experimental and computational analysis, Mater. Sci. Eng. C 70 (Jan 2017) 812–823.

[66] H.S. Ren, D. Liu, H.B. Tang, X.J. Tian, Y.Y. Zhu, H.M. Wang, Microstructure and mechanical properties of a graded structural material, Mater. Sci. Eng. A 611 (Aug 12, 2014) 362–369.

[67] Y. Liang, D. Liu, H. Wang, Microstructure and mechanical behavior of commercial purity Ti/Ti–6Al–2Zr–1Mo–1V structurally graded material fabricated by laser additive manufacturing, Scr. Mater. 74 (Mar 2014) 80–83.

[68] Jan Wieding, Robert Souffrant, Wolfram Mittelmeier, Rainer Bader, Finite element analysis on the biomechanical stability of open porous titanium scaffolds for large segmental bone defects under physiological load conditions, Med. Eng. Phys. 35 (4) (2012) 422–432.

[69] X. Liu, S. Chen, J.K.H. Tsoi, J.P. Matinlinna, Binary titanium alloys as dental implant materials—a review, Regen. Biomater. 4 (5) (Oct 2017) 315.

[70] G.M. Keegan, I.D. Learmonth, C.P. Case, Orthopaedic metals and their potential toxicity in the arthroplasty patient. A review of current knowledge and future strategies, J. Bone Joint Surg. Br. 89 (5) (2007) 567–573.

[71] J.J. Jacobs, A.K. Skipor, J. Black, R.M. Urban, J.O. Galante, Release and excretion of metal in patients who have a total hip-replacement component made of titanium-base alloy, J. Bone Joint Surg. Am. 73 (10) (1991) 1475–1486.

[72] Y. Nuevo-Ordóñez, M. Montes-Bayón, E. Blanco-González, J. Paz-Aparicio, J. Raimundez, J. Tejerina, et al., Titanium release in serum of patients with different bone fixation implants and its interaction with serum biomolecules at physiological levels, Anal. Bioanal. Chem. 401 (9) (Nov 2011) 2747–2754.

[73] X. Li, C.-T. Wang, W.-G. Zhang, Y.-C. Li, Properties of a porous Ti–6Al–4V implant with a low stiffness for biomedical application, Proc. Inst. Mech. Eng. H 223 (2) (Feb 1, 2009) 173.

[74] F. Kong, Y. Chen, D. Zhang, Interfacial microstructure and shear strength of Ti–6Al–4V/TiAl laminate composite sheet fabricated by hot packed rolling, Mater. Des. 32 (6) (2011) 3167–3172.

[75] D.C. Smith, S. Lugowski, A. McHugh, D. Deporter, P.A. Watson, M. Chipman, Systemic metal ion levels in dental implant patients, Int. J. Oral Maxillofac. Implants 12 (6) (Nov 1997) 828.

[76] J.A. Davidson, A.K. Mishra, P. Kovacs, R.A. Poggie, New surface-hardened, low-modulus, corrosion-resistant Ti-13Nb-13Zr alloy for total hip arthroplasty, Biomed. Mater. Eng. 4 (3) (1994) 231.

[77] C. Yue, B. Zhao, Y. Ren, R. Kuijer, H.C. van der Mei, H.J. Busscher, et al., The implant infection paradox: why do some succeed when others fail? Opinion and discussion paper, Eur. Cell. Mater. 29 (2015) 303–313.

[78] C.J. Wilson, R.E. Clegg, D.I. Leavesley, M.J. Pearcy, Mediation of biomaterial-cell interactions by adsorbed proteins: a review, Tissue Eng. 11 (1–2) (Jan 2005) 1–18.

[79] O.L.A. Harrysson, O. Cansizoglu, D.J. Marcellin-Little, D.R. Cormier, H.A. West, Direct metal fabrication of titanium implants with tailored materials and mechanical properties using electron beam melting technology, Mater. Sci. Eng. C 28 (3) (2008) 366–373.

[80] William Bonfield, Designing porous scaffolds for tissue engineering, Philos. Trans. R. Soc. A Math. Phys. Eng. Sci. 364 (1838) (Jan 15, 2006) 227–232.

[81] N. Taniguchi, S. Fujibayashi, M. Takemoto, K. Sasaki, B. Otsuki, T. Nakamura, et al., Effect of pore size on bone ingrowth into porous titanium implants fabricated by additive manufacturing: an in vivo experiment, Mater. Sci. Eng. C 59 (Feb 1, 2016) 690–701.